# MRF Technical Note # 49

# Can desert dust explain the anomalous greenhouse effect observed over the Sahara during July 2003 revealed by GERB/UM intercomparisons?

Jim M. Haywood, Richard P. Allan, Ian Culverwell, Tony Slingo,

Sean Milton, and John Edwards.

**Observational Research**
**Met Office**
**Cordouan 2**
**FitzRoy Rd**
**Exeter**
**Devon**
**EX1 3PB**

# MRF Technical Note # 49

# Can desert dust explain the anomalous greenhouse effect observed over the Sahara during July 2003 revealed by GERB/UM intercomparisons?

Jim M. Haywood[1], Richard P. Allan[2], Ian Culverwell[1], Tony Slingo[2], Sean Milton[1], and John Edwards[1].

[1]*Met Office, Exeter, UK.*

[2]*Environmental Systems Science Centre, University of Reading, Reading, UK.*

**Abstract.** Measurements of the top-of-the-atmosphere outgoing longwave radiation (*OLR*) for July 2003 from the new Geostationary Earth Radiation Budget instrument are used to assess the performance of the numerical weather prediction version of the Met Office Unified Model. A significant difference is found over desert regions of northern Africa where the model emits too much *OLR* by up to 40 $Wm^{-2}$ in the monthly mean. By cloud-screening the data we find an error of up to $50Wm^{-2}$ associated with cloud-free areas, which suggests an error in the model surface temperature, surface emissivity, or atmospheric transmission. By building up a physical model of the radiative properties of mineral dust based on in-situ, and surface-based and satellite remote sensing observations we show that the most plausible explanation for the discrepancy in *OLR* is due to the neglect of mineral dust in the model. The calculations suggest that mineral dust can exert a longwave radiative forcing by as much as $50Wm^{-2}$ in the monthly mean for 1200UTC in cloud-free regions, which accounts for the discrepancy between the model and the GERB observations. This suggests that inclusion of the radiative effects of mineral dust will lead to a significant improvement in the radiation balance of numerical weather prediction models with subsequent improvements in performance.

## 1. Introduction

The top of the atmosphere radiative energy balance between net incoming solar radiation and outgoing longwave radiation (OLR) is crucial in determining the large-scale atmospheric circulation and therefore the synoptic evolution important for weather and climate prediction. The launch of the new Geostationary Earth Radiation Budget (GERB) instrument on the Meteosat Second Generation (MSG) satellite in August 2002 has enabled new estimates of the accuracy of the broadband shortwave and longwave radiation budgets of general circulation models (GCMs) such as the numerical weather prediction (NWP) model of the Met Office, UK. The footprint from MSG instruments is centred on $0^oN$, $3.5^oW$ which means that the spatial resolution (approximately 45km by

40km at nadir) is particularly good over the African continent. In this study, GERB is used to assess the *OLR* of the NWP model.

While the representation of clouds in GCMs is generally considered to lead to the largest uncertainty in the longwave radiation budget and in weather and climate prediction models, here we present evidence for an error of comparable magnitude and spatial scale in the NWP model simulation of *OLR* associated with the neglect of the radiative effects of mineral dust aerosol. Section 2 describes the GERB observations and the NWP model. Section 3 compares the *OLR* from the model with the observations, and shows that differences in *OLR* from the model and GERB of up to 50Wm$^{-2}$ at 12UTC come from clear-sky regions. In section 4, we describe the radiation code and vertical profiles of temperature and humidity used in the NWP model and show that they are realistic. In section 5 we assess the surface skin temperature and model surface emissivity that would be needed to balance the clear-sky OLR discrepancy and show that these alone are unlikely to explain the differences. In sections 6 dust optical parameters are derived from a combination of in-situ measurements from the SaHAran Dust Experiment [e.g. *Tanré et al*., 2003] and remote sensing measurements from AErosol Robotic NETwork (AERONET) [*Holben et al*., 1998]. These are combined with satellite measurements of aerosol optical depth, $\tau_{aer}$, determined in section 7 to calculate the radiative effects of the mineral dust in section 8. A discussion and conclusion are presented in section 9.

## 2. Description of satellite and model OLR data.

Before comparing the measured and modelled *OLR*, it is informative to provide a brief description of the satellite data, the NWP model, and the radiation code used in the study.

### 2.1. Geostationary Earth Radiation Budget instrument (GERB)

The GERB instrument provides internally calibrated measurements of the shortwave and longwave broadband radiative energy budget at the top of the atmosphere. Because MSG operates in a geostationary orbit, radiation measurements covering the region approximately 60$^{o}$S-60$^{o}$N and 60$^{o}$E-60$^{o}$W are provided every 300 seconds, thereby offering excellent temporal resolution. The GERB pixel size of approximately 50 km is similar to the resolution currently used by many numerical weather prediction models. For further details of the GERB instrument see *Harries et al.* [2004]. In the present study we use preliminary data (Version 1) and manually correct for mis-registration of data and poor geo-location. For further details of the methodology see *Allan et al.* [2004].

### 2.2. The Numerical Weather Prediction version of the Unified Model

The numerical weather prediction (NWP) Unified Model used here is described in detail in *Allan et al.* [2004], but a brief description is given here. The basis for the current formulation of the operational global NWP Unified Model became operational in August 2002. The horizontal resolution is 0.83$^{o}$ longitude by 0.56$^{o}$ latitude (90km in the tropics) with 38 levels in the vertical. The non-hydrostatic dynamics is a two-time level semi-implicit, semi-Lagrangian formulation and is designed to conserve mass, mass weighted potential temperature, moisture and angular momentum. The data assimilation is the three dimensional variational assimilation scheme of *Lorenc* [2000]. Recent improvements have replaced the original initialisation procedure, and the incremental analysis update with a digital filtering technique.

For details on the layer-cloud and convective-cloud parameterisations, the land-surface exchange scheme, and orographic drag parameterisations see *Allan et al*. [2004]. The formulation of the global NWP model outlined above also forms the basis of the next generation coupled climate version (HadGEM1). The radiative transfer scheme in the NWP model is described in section 4, but it is important to note that the effects of aerosols in the longwave region of the spectrum are not accounted for.

## 3. Comparison of observed and modelled *OLR* budget.

In this section, we examine first the *OLR* from both GERB and the NWP models for both total sky conditions and then apply cloud-screening to look at the *OLR* for clear sky conditions, *OLRc*.

### 3.1 Comparison of monthly mean for July 2003.

The monthly mean *OLR* which is the mean of the 0, 6, 12, and 18UTC diagnostics for July 2003 is shown in Figure 1a and 1b for the GERB observations and the NWP model respectively and are henceforth referred to as $OLR_{GERB}$ and $OLR_{model}$. Figures 1a and 1b show the same general features over Africa. Both $OLR_{GERB}$ and $OLR_{model}$ are greater than 300Wm$^{-2}$ over hot, dry desert regions in the north and less than 220Wm$^{-2}$ over cold deep convective clouds of the inter-tropical convergence zone (ITCZ) in central equatorial Africa. Figure 1c shows the *dOLR* which is defined here as $OLR_{model}$ - $OLR_{GERB}$. The two most notable features over the African continent are:-

i) Significant negative bias associated with deep convective clouds of the ITCZ where $OLR_{model}<OLR_{GERB}$ and $|dOLR|$ exceeds 30Wm$^{-2}$.
ii) Significant positive bias over desert regions of northwest Africa where $OLR_{model}>OLR_{GERB}$ and $|dOLR|$ exceeds 30Wm$^{-2}$.

The *dOLR* associated with the ITCZ may be explained by systematic errors in the modelling of deep convective cloud and cirrus anvils. The complex issues of moisture transport, cloud microphysical parameterisations, cloud inhomogeneities, cloud overlap assumptions and the radiance to irradiance conversion performed by the GERB inversion procedures may all be important in explaining these discrepancies between the model and the observations. However, these issues associated with clouds are beyond the scope of the present study. Here, we concentrate on the significant positive bias over desert regions of northwest Africa. The fact that the bias in *dOLR* in this region is of similar magnitude and spatial extent to that associated with clouds of the ITCZ suggests that the model errors here are as significant in determining the *OLR* as those associated with modelling complex clouds. Furthermore, while the complex issues surrounding the accurate representation of cloud in models such as those listed above are well known but difficult to solve, the error over northwest Africa suggests either an error in the model parameterisations or a missing physical mechanism.

### 3.2 Application of cloud-screening.

To determine whether the bias in *dOLR* over northwest Africa is associated with cloudy or clear sky regions a cloud-screening procedure is applied whereby a pixel is considered cloud-free if the collocated data from GERB and from the NWP model are both classified as completely cloud-free. This avaoids the introduction of biases relating to inconsistent clear-sky sampling between model and satellite data [e.g. *Allan and Ringer*, 2003]. The GERB cloud product is provided by the Royal Meteorological Institute of Belgium and is based on the Meteosat cloud retrieval algorithm that was used in the GERB radiance to flux conversion [*Ipe et al.* 2004].

The clear-sky $OLRc_{GERB}$ and $OLRc_{model}$ for 12UTC are shown in Figures 2a and 2b respectively. It is important to realise that both $OLRc_{GERB}$ and $OLRc_{model}$ are effectively 'snapshots' and are therefore directly comparable: at $0^o$ longitude the local time is 12:00, but at $15^o$E the local time is 13:00 and at $30^o$E the local time is 14:00. The differences between $OLRc_{GERB}$ and $OLRc_{model}$ are more pronounced than in Figure 1, with $OLRc_{model}$ again showing considerably higher values across N. Africa than $OLRc_{GERB}$. *dOLRc*, which is defined as $OLRc_{model}$-$OLRc_{GERB}$, shows a maximum of greater than 30-50 $Wm^{-2}$ over Mali, Mauritania and Southern Algeria. The fact that *dOLRc* is so large indicates a deficiency in the clear-sky radiative transfer processes in the NWP model. The deficiency is unlikely to be associated with errors from the satellite retrieval given its large magnitude and spatial extent. Given that the error is unlikely to be associated with the GERB retrievals, the three most likely explanations for such a deficiency in $OLRc_{model}$ are misrepresentation of surface skin temperature, surface emissivity, atmospheric transmission, or a combination of the three. In the sections that follow, we describe the radiative transfer calculations and then investigate the potential error in skin temperature and emissivity that would lead to *dOLRc* and compare the results against available observations. We then investigate the radiative processes associated with atmospheric mineral dust.

## 4. Description of the radiative transfer calculations

Here we describe the physical basis of the radiative transfer code and the temperature and humidity profiles that are used as input to the code to derive the OLR.

### 4.1 The physical basis of the radiative transfer code.

The radiative transfer code used in this study is that of *Edwards and Slingo* [1996] which is based on the two-stream equations in both the long-wave and short-wave spectral regions which allows for consistency in physical processes which are important in both spectral regions. Atmospheric absorption by water vapour, carbon dioxide, ozone, oxygen, nitrous oxide, methane and CFC-11 and CFC-12 are accounted for. The scheme includes a treatment of Rayleigh scattering, non-spherical ice particles, and multiple scattering between cloud layers, and includes scattering and absorption by aerosols.

The spectral resolution of the radiation code is variable; in the NWP model, there are 6 bands in the shortwave spectrum and 9 bands in the longwave spectrum. In addition, we use a 300 band stand alone version in calculations of the effects of surface skin temperature, surface emissivity and aerosol upon the longwave irradiances, and a 220 band stand alone version in calculations of the solar irradiances. These higher spectral resolution versions of the radiation code have previously been used for calculations of the shortwave and longwave radiative effects of mineral dust aerosol by *Haywood et al.* [2001; 2003a] and *Highwood et al.* [2003].

### 4.2 Vertical profiles of temperature and humidity

The OLR is a strong function of the atmospheric temperature and humidity, and therefore it is necessary to use appropriate atmospheric profiles in radiative transfer calcualtions. However, observational data is extremely sparce over the Sahara Desert. In this study, we use radiosonde ascents from three nearby bases in southern Algeria located at In Salah, Tindouf, and Tamanrasset (see Figure 2c). The radiosonde ascents shown in Figure 3a-c consist of monthly mean data from the mid-day radiosonde launches. The atmospheric profiles show characteristics typical of that shown by *Thorncroft et al.* [2003] during the JET-2000 measurement campaign shown in Figure 3d (location also marked on Figure 2c). Although there are differences between the profiles, particularly close to the surface, the following general features can be seen:-

i) From the surface to ~550hPa, the profile of atmospheric temperature is close to the dry adiabatic lapse rate.
ii) Typically, the temperature of the air close to the surface is ~315K, and because the atmospheric profile is close to dry adiabatic, the equivalent potential temperature is approximately constant up to ~550hPa .
iii) From the surface to ~550hPa the specific humidity is typically 2-4gcm$^{-3}$.

We use the atmospheric profile from observations at In-Salah in the radiative transfer calculations that follow. Use of the profiles from Tindouf and Tamanrasset changes the *OLRc* by less than 2Wm$^{-2}$. Also plotted on Figure 3 are the NWP monthly mean model analyses of temperatures and humidities for 12UTC. Because the NWP model uses data assimilation including data from radiosondes [section 2.2], the model profiles of temperature and humidity are in very close agreement with the radiosonde assents (Figures 3a-c). Calculations using the NWP model profiles of temperature and humidity for In Salah lead to differences in *OLRc* of less than 3Wm$^{-2}$ when compared to those using the observations. Thus the model profiles of temperature and humidity cannot be responsible for the *dOLRc* shown in Figure 2c.

## 5. Investigation of surface skin temperature and emissivity.

### 5.1. Surface skin temperature, Ts

The surface skin temperature for 12UTC from the NWP model $Ts_{model}$, is shown in Figure 4a. The region of maximum $Ts_{model}$ approximately correspond to the region where *OLRc* is largest (Figure 2b) and is somewhat displaced to the north from the region that shows the maximum *dOLRc* (Figure 2c). The maximum $Ts_{model}$ exceeds 330K. We use the 300 band version of the *Edwards and Slingo* [1996] radiation code to investigate the perturbation to the surface temperature, dTs, needed to reconcile $OLRc_{GERB}$ and $OLRc_{model}$ i.e. to reduce *dOLRc* to zero. Figure 4b shows dTs and Figure 4c shows

$Ts_{model}$+dTs. Figure 4b shows that $Ts_{model}$ needs to be reduced by up to -30K in order for $OLRc_{GERB}$ and $OLRc_{model}$ to agree resulting in a Ts ~310K in the region where the maximum *dOLRc* exists.

To determine whether potential errors in Ts are the reason for the discrepancy in *OLRc* it is necessary to assess whether $Ts_{model}$ (Figure 4a) or $Ts_{model}$+dTs (Figure 4c) provides the best representation of the real Ts. Physical measurements of Ts over desert regions are extremely sparse and therefore remote sensing measurements from satellite sensors are frequently used. The International Satellite Cloud Climatology Project (ISCCP) dataset indicates a *diurnal mean* July surface skin temperature determined from satellite measurements from the period 1982-2001 (Prigent et al., 2003; see http://isccp.giss.nasa.gov) under clear sky conditions in excess of 314K over the Sahara desert. The monthly mean Ts from the model for the grid-box including In Salah is shown in Figure 5 by the data points and standard deviations at three hourly intervals. Ts from Tamanrasset, Tindouf, and other model grid-points shows similar features and are not shown here. The diurnal mean Ts is approximately 312-313K, which is in agreement with the ISCCP climatological data. In addition, the model shows a diurnal cycle that is in agreement with observational data from Meteosat Ts data analysed by Gottsche and Oleson [2001] who fitted observational data from the Algerian desert with a cosine and exponential decay term. The fit from this parameterisation and the coefficients used in fitting the parameterisation are also shown on Figure 5, which shows agreement with the model data. Prigent et al [2003] also present data from desert regions and document that Ts is larger than the near-surface air temperature by approximately 10-14K close to local noon. If we consider that the maximum Ts at In Salah, Tamanrasset, and Tindouf from the model are around 330K (Figure 4a, and Figure 5), then the near surface air temperature would be expected to be around 318K or around 45C. The monthly-mean near surface air temperature shown in the tephigrams in Figure 3 is around 40-43C which shows reasonable agreement. These facts suggest that the model Ts is reasonably realistic, and is not significantly in error.

### 5.2. Surface emissivity, ε

To investigate the effect of non-unity surface emissivity, ε, on the *OLRc*, the radiative transfer calculations are repeated using a broadband ε of 0.95 and 0.90 in place of the ε of 1.0. ISCCP report an emissivity of barren desert regions of around 0.95 for the 5-200μm spectral region and around 0.98 for the 10-11μm spectral region. *Sutherland* [1986] suggests similar values for ε and thus the radiative transfer calculations with ε=0.90 can be considered an extreme. The results indicate a reduction in *OLRc* of approximately $7Wm^{-2}$ when ε is reduced from 1.0 to 0.95, and $14Wm^{-2}$ when ε is reduced from 1.0 to 0.90 for a surface temperature of 330K. Thus it appears unlikely that differences in ε can explain the magnitude of *dOLRc* shown in Figure 2c which exceeds $50Wm^{-2}$ in some regions.

## 6. Mineral dust aerosol.

Having determined that model errors in Ts and ε are unlikely to explain *dOLRc* we now investigate the final possibility; that the atmospheric transmission in the NWP model is in error. As we have seen that the model atmospheric temperature and humidity are well represented in the model as evidenced by the tephigrams shown in Figure 3, we concentrate on the radiative effects of aerosols and their effect on *OLRc*.

### 6.1 Aerosol size distributions.

As in *Highwood et al.* [2003], two independent types of measurements of size distributions are combined with aerosol refractive indices across the solar and terrestrial spectra to determine the optical properties. The first data set is the in-situ observations made on the Met Office C130 aircraft with a Passive Cavity Aerosol Spectrometer Probe 100-X (PCASP) during a large dust event off the coast of Senegal during the SaHAran Dust Experiment [SHADE; *Tanré et al.,* 2003]. The approximate geographical position of the measurements made during SHADE is marked on Figure 2c. Briefly, the PCASP sizes aerosols in the radius range 0.05-1.5μm by measuring the intensity of laser radiation of wavelength 0.63μm at scattering angles of between $35^{o}$ and $120^{o}$. *Haywood et al.*, 2003a and *Haywood et al*., 2003b provide details of the calibration, and potential sizing errors of the PCASP. In this study, the main limitation of using data from the PCASP is the maximum detection radius of 1.5μm which enables determination of the aerosol radiative properties of at solar wavelengths but is too small for accurate determination of radiative properties at terrestrial wavelengths [e.g. *Haywood et al.*, 2003a; *Highwood et al*., 2003]. This necessitates the use of supplemental aerosol size distribution data from the AERONET station at Dahkla in Mauritania (geographically the closest AERONET station to the maximum in *dOLRc* as shown on Figure 2). The monthly mean aerosol size distribution for July 2003 is derived using the retrieval algorithm of *Dubovik and King* [2000]. Briefly, this inversion procedure minimises the RMS error between measured and modelled sky radiances as a function of scattering angle at a range of wavelengths. The main disadvantage of this retrieval algorithm for mineral dust particles is that non-spherical scattering effects lead to an anomalous peak in the aerosol size distribution at sizes of <0.1μm. However, this effect is well-understood and can be corrected for using a composite of prolate and oblate spheroids in place of spheres [*Dubovik et al*., 2002].

We show the volume size distribution of the aerosol size distribution from the PCASP and the AERONET retrievals in Figure 6. Other than the anomalous peak in the AERONET size distribution at particle radii <0.1μm, the size distribution from the SHADE campaign and the AERONET retrieval are in remarkable agreement when one considers the different geographical locations, the different time of year of the sampling, and the different methods for retrieving the aerosol size distribution. The composite PCASP/AERONET size distribution may be fitted with five log-normal modes as shown in Figure 6; the standard deviation and geometric mean radius of each of these modes are identical to those in *Haywood et al.* [2003a]. A further mode fitting particles greater than 10μm radius could be included but tests show that this mode has negligible effect on the optical parameters and hence negligible effect on the radiative effects across the solar and terrestrial regions of the spectrum.

### 6.2. Aerosol optical properties.

The composite size distribution shown by the solid line in Figure 6 is combined with suitable refractive indices and Mie scattering theory to determine the aerosol optical parameters. As in *Highwood et al.* [2003], we use the refractive indices of *WCP* [1986] for wavelengths less than 4.5μm. However, the refractive indices of *WCP* [1986] do not adequately represent the optical characteristics of Saharan dust at terrestrial wavelengths as evidenced by interferometer measurements [*Highwood et al.*, 2003]. The refractive indices of *Volz et al.* [1973] and *Fouquart et al.* [1987] both show a stronger absorption peak at around 10μm due to the presence of illite and are more representative of the spectral dependence of the absorption of Saharan dust across the terrestrial spectrum [*Highwood et al.*, 2003]. Therefore, we replace the refractive indices of *WCP* [1986] at wavelengths greater than 2.5μm with those of *Volz et al.* [1973].

Figure 7a-c shows the specific extinction coefficient, $k_e$, the single scattering albedo, $\omega_o$, and the asymmetry factor, $g$, derived using the size distribution shown in Figure 7 and the combined refractive indices of *WCP* [1986] and *Volz et al.* [1973]. The crosses marked on Figure 7a show the variation of $\tau_{aer\lambda}$ from the Dahkla AERONET site. These data have been normalised so that $\tau_{aer0.55}$~$k_{e0.55}$ in order to demonstrate that the wavelength dependence of $k_e$ is well represented despite the fact that monthly mean aerosol size distribution and refractive indices are used in the Mie scattering calculations while the AERONET values are determined from the mean of the daily $\tau_{aer}$. Additionally, Figure 7b shows that $\omega_o$ calculated from the mean of the daily AERONET size distributions is in good agreement with those calculated using the monthly mean size distribution and the assumed refractive indices. This consistency suggests that the use of a single monthly mean size distribution and set of refractive index is justified.

### 6.3 Geographic distribution of mineral dust aerosol.

Many different satellite instruments have been developed that determine $\tau_{aer\lambda}$ and aerosol properties such as Angstrom coefficients and radiative effects [e.g. *Myhre et al.,* 2003]. The majority of these satellite retrievals are capable of determining aerosol radiative effects over ocean, but retrieval algorithms for the Total Ozone Mapping Spectrometer [TOMS; *Herman et al*., 1997] and the Multiangle Imaging SpectroRadiometer [MISR; *Diner et al.*, 2001] are also capable of determining aerosol radiative effects over highly reflectant land surfaces such as desert.

In this study, we use the TOMS Aerosol Index (AI) which provides a measure of the column integrated atmospheric burden of partially absorbing atmospheric aerosols. The TOMS AI does not translate to $\tau_{aer}$ via a universal linear relationship, as it is dependent on the aerosol absorption properties and the altitude of the aerosol. *Hsu et al.* [1999] compared $\tau_{aer0.44}$ data from six AERONET sites in N.W. Africa to TOMS AI and reported a linear relationship for each site. Here, we use data from the two geographically most representative sites of Dakar and Cape Verde (close to the area marked SHADE on Figure 2c) and infer from the study of *Hsu et al.* [1999] that :-

$$\tau_{aer0.44}=0.35(\text{TOMS AI})+0.095 \qquad (1)$$

$\tau_{aer\lambda}$ is deduced at all wavelengths by assuming that the size distribution shown in Figure 6 is representative of typical atmospheric dust size distributions, leading to the wavelength dependency of $k_{e\lambda}$ shown in Figure 7 which is linearly related to $\tau_{aer\lambda}$. $\tau_{aer\lambda}$ is normally reported at 0.55µm and so we infer:-

$$\tau_{aer0.55}=0.98\,\tau_{aer0.44}=0.34(\text{TOMS AI})+0.093 \qquad (2)$$

We also infer that:-

$$\tau_{aer10}=0.52\,\tau_{aer0.55} \qquad (3)$$

which is useful in comparing $\tau_{aer}$ for solar and terrestrial wavelengths.

Monthly mean TOMS AI are constructed from the daily TOMS AI data (website: http://toms.gsfc.nasa.gov/aerosols/aerosols.html) and rescaled to the NMP model grid. These data are converted from the semi-quantitative TOMS AI to $\tau_{aer0.55}$ by using the relationships detailed in Eq (1) and Eq (2). The TOMS $\tau_{aer0.55}$ for July 2003 is shown in Figure 8a. $\tau_{aer0.55}$ shows a maximum over regions of the Sahara centred on approximately $20^o$N, $5^o$W where $\tau_{aer0.55}$ exceeds 1.4.

TOMS AI data has the advantage that data is available over both land and ocean since 1978. However, dedicated aerosol instruments have been developed in recent years that determine $\tau_{aer0.55}$ over land. MISR is one such instrument and its multi-angle viewing capability enables determination of $\tau_{aer0.55}$ even over bright desert surfaces [e.g. *Zhang and Christopher*, 2003]. The monthly mean MISR $\tau_{aer0.55}$ for July 2003 is shown in Figure 8b.

Comparison of Figure 8a and 8b reveals the same general spatial distribution of $\tau_{aer0.55}$ but the TOMS data is much more diffuse than the MISR data. This is because the swath width from the TOMS instrument is relatively wide (3100km) and consequently every area on the globe is sampled each day. MISR has a superior resolution, but a narrow swath width (360km) which means that sampling over the region typically occurs once every five to six days. In addition, MISR does not retrieve $\tau_{aer0.55}$ in the presence of clouds. Nevertheless, we transform the TOMS $\tau_{aer0.55}$ and MISR $\tau_{aer0.55}$ onto the NWP model grid and perform a correlation between the two. The resulting scatter-plot is shown in Figure 9 which shows a large amount of scatter. Much of this scatter is due to the poorer sampling statistics for MISR; the spatial inhomogeneity of Saharan dust plumes is extreme [e.g. *Tanré et al.*, 2003] so MISR may miss dust events at certain locations altogether. The following approximate linear relationship may be derived:-

$$\text{TOMS }\tau_{aer0.55} = (1.00\pm0.28)(\text{MISR }\tau_{aer0.55})-(0.02\pm0.12)\ \ (r=0.75) \qquad (4)$$

Because the sampling statistics are better for TOMS $\tau_{aer0.55}$ and because the agreement between TOMS $\tau_{aer0.55}$ and MISR $\tau_{aer0.55}$ is 1:1 (rather fortuitously considering the magnitude of the estimated error), we use TOMS $\tau_{aer0.55}$ in the calculations that follow in section 8.

Comparison of the TOMS $\tau_{aer0.55}$ shown in Figure 8a with the *dOLRc* shown in Figure 2c indicates that there is a reasonable correlation between the two. However, correlation alone does not establish cause and effect and the effects of aerosol on the *OLR* are investigated in a more rigorous manner in the sections that follow.

The vertical profile of mineral dust is deduced from the measurements made by *Haywood et al.* [2003a]. These measurements were performed off the coast of West Africa during SHADE (see Figure 2c for the geographical position), and revealed the presence of a shallow, dust-free marine boundary layer below the mineral dust layer which had a clearly defined top at 500-600hPa correlated to a strong hydrolapse. The hydrolapse shown in Figures 3a-c occurs at a pressure of approximately 550hPa, and therefore we apply a constant mass mixing ratio of mineral dust aerosol from the surface to 550hPa. Such profiles have been shown to be representative over arid land surfaces where the strong surface heating causes strong vertical mixing and therefore well-mixed specific humidity as shown in Figure 3 [*Haywood et al*., 2003a; 2003c].

## 7. Direct radiative effects of mineral dust.

While it would be possible to estimate the effect of aerosols on the *OLRc* by applying them directly to the NWP UM, here we choose to use an off-line version of the *Edwards and Slingo* [1996] radiative transfer code. The advantage of this approach is one of flexibility; the aerosol optical properties, concentrations and atmospheric profiles of temperature and humidity may be adjusted much more readily than in the full NWP model. The disadvantage of this approach is that the dynamical feedbacks due to aerosols affecting the radiation budget are difficult to assess. Nevertheless, the off-line radiative transfer modelling approach presented here is an important step in identifying whether the inclusion of aerosols within the NWP model are capable of explaining the *dOLRc* diagnosed in section 3.2.

Because we are primarily interested in the cause of *dOLRc*, we first investigate the effect of aerosols directly upon *OLRc* by calculating the direct radiative effect in the longwave region of the electromagnetic spectrum, $DRE_{LW}$. We estimate the clear-sky $DRE_{LW}$ as the difference between the top of the atmosphere *OLRc* with and without aerosols, i.e. $DRE_{LW}=OLRc_{no\_aer}-OLRc_{aer}$. $OLRc_{no\_aer}$ and $OLRc_{aer}$ are estimated using the *Edwards and Slingo* [1986] radiative transfer code. Aerosols also exert a significant perturbation to the solar radiation as evidenced by measurements of large values of $DRE_{SW}$ at the top of the atmosphere [e.g. *Haywood et al.*, 2003a]. Aerosols reduce the solar radiation at the surface through a combination of scattering solar radiation back to space, and absorption of radiation leading to a significant direct radiative effect at the surface $DRE_{SW\_surf}$. The reduction in the solar radiation at the surface will reduce the surface temperature, which will in turn further reduce the *OLR*. Thus, through land-surface feedback processes, the $DRE_{SW}$ induces a $DRE_{LW}$. Here we define $DRE_{LWfeedback}$ as the additional perturbation to the *OLR* caused by the feedback effects of the $DRE_{SW}$ on the surface temperature.

### 7.1. Calculations of $DRE_{LW}$

The atmospheric profiles of temperature and humidity used as inputs to the radiative transfer code are the monthly-mean radiosonde ascent from In Salah described in section 4, and the vertical profile of aerosol is described in section 7. Concentrations of all other atmospheric gases are set to 2003 atmospheric values. The radiative transfer calculations are performed for surface temperatures ranging from 280-340K, and for $\tau_{aer0.55}$ ranging from 0-1.5 ($\tau_{aer10}$ ranging from 0-0.78) to form a look-up-table shown graphically in Figure 10.

Figure 10 shows that in the absence of aerosol $OLRc_{no\_aer}$ ranges from approximately 284-406Wm$^{-2}$ for a surface temperature ranging from 280-340K. These values encompass those shown in Figure 2b indicating that the radiative transfer calculations are representative of those in the NWP model. When $\tau_{aer0.55}$=1.5, $OLR_{aer}$ ranges from 280-353 Wm$^{-2}$ for the same range in surface temperature. Thus the $DRE_{LW}$ for $\tau_{aer0.55}$=1.5 ranges from 4 Wm$^{-2}$ at 280K to 53 Wm$^{-2}$ at 340K. If $\tau_{aer0.55}$=1.0, which is reasonable for areas of the western Sahara desert (see Figure 8), then $DRE_{LW}$ is 25 Wm$^{-2}$, 32 Wm$^{-2}$, and 39Wm$^{-2}$ for surface temperatures of 320K, 330K, and 340K.

Figure 11 shows the $DRE_{LW}$ calculated from the look-up-table and using the monthly mean surface temperatures of Figure 4a and the $\tau_{aer0.55}$ from Figure 8a re-gridded onto the model grid. The data have been cloud-screened using the identical mask to that described in section 3.2 so they are directly comparable. Comparison of Figure 11 with Figure 2c reveals a similar general geographical pattern, $DRE_{LW}$ is somewhat smaller in magnitude than *dOLRc* by some 20-30%. Thus, although inclusion of mineral dust in the terrestrial spectrum produces a $DRE_{LW}$ that goes a long way to explaining the *dOLRc*, it appears that $DRE_{LW}$ alone does not fully account for the discrepancy.

### 7.2. Calculations of $DRE_{LWfeedback}$

To estimate the effect that the presence of mineral dust has upon the solar radiation budget at the surface, the surface temperature and hence on *OLRc*, the *Edwards and Slingo* [1996] radiation code was run using 220-bands across the solar spectrum. Gaseous and aerosol atmospheric constituents were treated in a manner consistent with the radiative transfer calculations detailed in section 8.1. Radiative transfer calculations were performed with and without mineral dust aerosol for a range of $\tau_{aer0.55}$ and solar zenith angles. The Lambertian surface reflectance is set to a wavelength and solar zenith angle independent value of 0.30 which is typical of desert surfaces. The downwelling irradiance at the surface without aerosols, $SW_{surf\_no\_aer}$, and with aerosols, $SW_{surf\_aer}$, are then calculated (Figure 12).

The Gottsche and Olesen [2001] parameterisation (Section 5.1, and Figure 5) is fitted to the model data at each model grid-point. Because the primary controller of the diurnal cycle is the irradiance at the surface (or the cosine of the solar zenith angle, see Figure 5) we then make the reasonable assumption that, in clear skies, the diurnal cycle of Ts is damped by the ratio of $SW_{surf\_aer}/SW_{surf\_no\_aer}$. For a solar zenith angle of 20°, $SW_{surf\_no\_aer}$ is approximately 1060Wm$^{-2}$ while $SW_{surf\_aer}$ is 855Wm$^{-2}$ for a $\tau_{aer0.55}$ of 1. Thus, in this case, the damping in the diurnal range in temperature is a factor of approximately 0.81. The change in Ts at 12UTC calculated in this way indicates a cooling in of up to approximately 10K.

Once the change in the Ts due to the radiative effects of dust in the solar spectrum has been calculated, the look-up-table shown in Figure 10 is used to calculate $DRE_{LWfeedback}$ which is shown in Figure 13. Comparison of $DRE_{LWfeedback}$ and $DRE_{LW}$ reveals that $DRE_{LWfeedback}$ is approximately 25% of $DRE_{LW}$ and is therefore a second order effect.

Figure 14 shows the combined estimate of the effect of $DRE_{LW}$+ $DRE_{LWfeedback}$ which is our best estimate of the effect of mineral dust on *OLRc*. Comparison of $DRE_{LW}$+ $DRE_{LWfeedback}$ (Figure 14) with *dOLRc* (Figure 2c) reveals the radiative effects of mineral dust can indeed explain much of the discrepancy between the observations of *OLRc* from GERB and those from the NWP model.

## 9. Discussion and Conclusions

New geostationary satellite measurements show a significantly stronger atmospheric greenhouse effect over cloud-free desert regions of N.W. Africa than simulated by the Met Office NWP model. Monthly mean clear-sky *OLRc* from GERB satellite data is up to 50 Wm$^{-2}$ lower than model estimates during July 2003 when considering collocated 1200 UTC data. The available evidence suggests that the surface temperature and emissivity are unlikely to explain these differences. By building up a physically realistic model of the radiative properties of mineral dust and applying aerosol burdens that are derived from satellite instruments, we show that inclusion of the radiative effects of mineral dust is a plausible mechanism for reconciling the differences between GERB measurements and the NWP model.

There are a few caveats regarding the current study. For example, the lack of knowledge of the terrestrial refractive indices of mineral dust in the region is potentially a large source of error. If the refractive indices of *Fouquart et al.* [1987] are used instead of those of *Volz* [1973], then the $DRE_{LW}$ is reduced. Calculations show that for a Ts of 330K and a $\tau_{aer0.55}$=1.0, $DRE_{LW}$ is 36.8Wm$^{-2}$ using the Volz et al. [1973] refractive indices, but reduced to 24.6Wm$^{-2}$ using the Fouquart [1987] refractive indices. Additionally, the exact details of the large modes of the aerosol size distribution from AERONET used in determining the radiative properties of mineral dust may not be entirely accurately characterised. This is because the AERONET radiometers measure the angular distribution of scattered radiances up to a wavelength of approximately 1μm. According to Mie scattering theory particles interact most effecitively with radiation when the radius of the aerosol particles is approximately the wavelength of the incident radiation. Thus radiances at 1μm are not very sensitive to aerosols of 10μm radius, leading to potential errors in the AERONET derived size distribution at large radii. The assumption of spherical particles should not influence the radiative properties of the aerosol in the terrestrial region of the spectrum to a large extent. It is also acknowledged that the assumption of constant aerosol mass mixing ratio in the vertical is crude, but validation data is lacking. The estimation of dTs due to the presence of mineral dust calculated here may not be entirely accurate because we consider only the effect of the aerosol on the solar radiation at the surface. There will be a further effect on Ts caused by the absorption and the re-emission of terrestrial radiation by dust that will increase Ts, although this effect is probably most important in increasing the night-time minimum Ts.

There are only a few studies that have investigated the effect of mineral dust on LW irradiances over land regions. The most directly comparable study to that presented here is that of *Zhang and Christopher* [2003], who used MISR $\tau_{aer0.55}$ and LW irradiances from the Clouds and Earth's Radiant Energy System [CERES; *Wielicki et al.*, 1996] to investigate $DRE_{LW}$ of Saharan dust over desert surfaces and derived a normalised $DRE_{LW}$ over western Africa of 20Wm$^{-2}$/$\tau_{aer0.55}$. However, as shown by Figure 10, $DRE_{LW}$ will be a strong function of surface temperature and because the Terra satellite overpasses used in their study will be from approximately 10UTC, the surface temperature will be somewhat lower than in our study (Figure 5 suggests approximately 10K lower) leading to a lower value of $DRE_{LW}$. It is therefore more appropriate to compare the results from the sensitivity calculations of *Zhang and Christopher* [2003]. In these tests, they use the dust model from *Hess et al.* [1998] to determine the normalised $DRE_{LW}$ for different aerosol scale heights, surface temperatures and atmospheric precipitable water. They perform calculations for an aerosol scale height of 2km, a surface temperature of 316K, and a precipitable water content of 1.6cm and determine a normalised $DRE_{LW}$ of 18.7Wm$^{-2}$/$\tau_{aer0.55}$. The precipitable water from the radiosonde at In Salah is approximately 1.2cm, and analysis of Figure 10 reveals a corresponding normalised $DRE_{LW}$ of 22.2Wm$^{-2}$/$\tau_{aer0.55}$. Given the sensitivity of $DRE_{LW}$ to the precipitable water shown by *Zhang and Christopher* [2003], these results are in good agreement. The diurnal cycle of surface temperature means that there is a diurnal cycle in $DRE_{LW}$. Using the Ts data shown in Figure 5, a diurnally averaged mean $DRE_{LW}$ is 20.6Wm$^{-2}$ for a $\tau_{aer\lambda=0.55}$ of 1.0 is calculated while the corresponding maximum and minimum $DRE_{LW}$ are 30.3Wm$^{-2}$ and 13.8Wm$^{-2}$. No changes in the atmospheric profile of temperature or humidity are accounted for in this estimate.

To conclude, this study shows that neglecting the radiative effects of mineral dust, may lead to the largest error in the NWP model estimates of the TOA OLR budget that is observed in the GERB footprint. Further studies where mineral dust is incorporated directly into NWP models are planned and these should be able to assess the effect of mineral dust on the local and regional meteorology and climate.

**Acknowledgements.** John Foot, Pete Francis, and Doug Parker are thanked for useful discussions. Jean-Claude Thelen is thanked for maintaining the radiation code used in this study. The NASA GSFC TOMS team are thanked for making Aerosol Index data available, and the NASA Langley Research Center are thanked for making the MISR data available. The work was part funded by the joint NERC/Met Office Connect-B grant NER/D/S/2002/00412.

## References

Allan, R.P. et al., manuscript in preparation, 2004.

Allan, R. P. and M. A. Ringer, Inconsistencies between satellite estimates of longwave cloud forcing and dynamical fields from reanalyses, *Geophys. Res. Lett*., 30(9), 1491, doi:10.1029/2003GL017019, 2003.

Boucher, O., … et al., 1998. Intercomparison of models representing direct shortwave radiative forcing by sulfate aerosols. *Journal of Geophysical Research*, 103, 16979-16998.

Diner D.J., W.A. Abdou, J.E. Conel, K.A. Crean, B.J. Gaitley, M. Helmlinger, R.A. Kahn, J.V. Martonchik, and S.H. Pilorz, MISR aerosol retrievals over southern Africa during the SAFARI-2000 dry season campaign, *Geophys Res Lett*., 28, 31227-3130, 2001.

Dubovik, O and M.D. King, A flexible inversion algorithm for retrieval of optical properties from Sun and sky radiance measurements, J. Geophys. Res., 105, 20-673-20, 696, 2000.

Dubovik, O., B.N. Holben, T. Lapyonok, A. Sinyuk, M.I. Mishchenko, P. Yang and I. Slutsker, Non-spherical aerosol retrieval method employing light scattering by spheroids, Geophys. Res. Letts, ,29, 2002.

Edwards, J.M., and A. Slingo, Studies with a flexible new radiation code. I: Choosing a configuration for a large scale model, Q. J. R. Meteorol. Soc., 122, 689-720, 1996.

Harries, J.E., et al., The Geostationary Earth Radiation Budget experiment (GERB), under preparation.

Haywood, J.M., Osborne, S.R., Francis, P., Glew, M., Highwood, E., Formenti, P., and Andreae, M., Radiative properties and direct radiative effect of Saharan dust measured by the C-130 aircraft during SHADE: 1. Solar spectrum, *Journal of Geophysical Research*, 8577, doi:10.1029/2002JD002687, 2003a.

Haywood, J.M., Francis, P.N., Glew, M.D., Dubovik, O., and Holben, B.N, Comparison of aerosol size distributions, radiative properties, and optical depths determined by aircraft observations and Sun photometers during SAFARI-2000. *Journal of Geophysical Research*, 108(D13), 8471, doi:10.1029/2002JD002250, 2003b.

Haywood, J.M., Osborne, S.R. Francis, P.N., Keil, A., Formenti, P., Andreae, M.O., and Kaye, P.H., The mean physical and optical properties of regional haze dominated by biomass burning aerosol measured from the C-130 aircraft during SAFARI 2000, Journal of Geophysical Research, 108(D13), 8473, doi:10.1029/2002JD002226, 2003c.

Haywood, J.M., Francis, P.N., Glew, M.D., and Taylor, J.P.. Optical properties and direct radiative effect of Saharan Dust: A case study of two Saharan dust outbreaks using aircraft data. J. Geophys. Res., 106, 18,417-18428, 2001.

Hsu, N.C., Herman, J.R., Torres, O., Holben, B.N., Tanré, D., Eck, T.F., Smirnov, A., Chatenet, B., and Lavenu, F., Comparison of the TOMS aerosol index with Sun-photometer aerosol optical thickness: Results and applications, J. Geophys. Res., 104, D6, 6269-6279, 1999.

Fouquart, Y., B. Bonnel, G. Brogniez, J.C. Buriez, L. Smith, J.J. Morcrette, Observations of Saharan aerosols: results of ECLATS field experiment. Part II: Broadband radiative characteristics of aerosols and vertical flux divergence, *Jour. Clim. And Appl. Meteorol.*, 26, 38-52, 1987.

Göttsche, F.-M., and Olesen, F.-S., Modelling of diurnal cycles of brightness temperature extracted from METEOSAT data. Remote Sens. Environ., 76(3): 338-349, 2001.

Herman, J.R., P.K. Bhartia, O. Torres, C. Hsu, C. Seftor, and E. Celarier, Global distribution of UV-absorbing aerosols from Nimbus 7/TOMS data, J. Geophys Res., 102, 16911-16922, 1997.

Hess, M., P. Koepke, and I. Schult, 1998. Optical properties of aerosols and clouds: the software package OPAC, Bull. Am. Met. Soc., 1998.

Highwood, E.J., Haywood, J.M., Silverstone, M.D., Newman, S.M., and Taylor, J.P., 2003. Radiative properties and direct effect of Saharan dust measured by the C-130 aircraft during SHADE. 2: Terrestrial spectrum. *Journal of Geophysical Research,* 108(D18), 8578, doi:10.1029/2002JD002552, 2003.

Holben, B.N., et al., AERONET: A federated instrument network and data archive for aerosol characterization. Remote Sens. Environ., 66, 1-16, 1998.

Ipe, A., N. Clerbaux, C. Bertrand, S. Dewitte, and L.Gonzalez, 2004. Validation and homogenisation of cloud optical depth and cloud fraction retrievals for GERB/SEVIRI scene identification using Meteosat-7 data, Atmospheric Research, submitted.

Lorenc, A. C. and Ballard, S. P. and Bell, R. S. and Ingleby, N. B. and Andrews, P. L. F. and Barker, D. M. and Bray, J. R. and Clayton, A. M. and Dalby, T. D. and Dingmin, LI. and Payne, T. J. and Saunders, F. W., The Met. Office global three-dimensional variational data assimilation scheme, *Q. J. R. Meteorol. Soc*., 126, 570, 2991-3012, 2000.

Mishchenko, M. I., I. V. Geogdzhayev, L. Liu, J. A. Ogren, A. A. Lacis, W. B. Rossow, J. W. Hovenier, H. Volten, and O. Muñoz, Aerosol retrievals from AVHRR radiances: effects of particle nonsphericity and absorption and an updated long-term global climatology of aerosol properties, *J. Quant. Spectrosc. Radiat. Transfer* 79/80, 953-972, 2003.

Myhre, G., F. Stordal, M. Johnsrud, A. Ignatov, M. I. Mishchenko, I. V. Geogdzhayev, *et al.*, Intercomparison of satellite retrieved aerosol optical depth over the ocean, *J. Atmos. Sci,*. 61, 499-513, 2004.

Prigent C., F. Aires, W. B. Rossow, Land surface skin temperatures from a combined analysis of microwave and infrared satellite observations for an all-weather evaluation of the differences between air and skin temperatures, J. Geophys. Res., 108 (D10), 4310, doi:10.1029/2002JD002301, 2003.

Sokolik, I.N., O.B. Toon and R.W. Bergstrom, Modelling the radiative characteristics of airborne mineral aerosols at infrared wavelengths, J. Geophys. Res., 103, 8813-8826, 1998.

Sutherland, R. A., Broadband and Spectral Emissivities (2-18 um) of Some Natural Soils and Vegetation. *Journal of Atmospheric and Oceanic Technology*: Vol. 3, No. 1, pp. 199-202, 1986.

Tanré, D., J.M. Haywood, J. Pelon, J.F., Léon, B. Chatenet, P. Formenti, P. Francis, P. Goloub, E.J. Highwood, and G. Myhre, Measurement and modeling of the Saharan dust radiative impact: overview of the SaHAran Dust Experiment (SHADE), *Journal of Geophysical Research*, 8574*,* 108(D13), doi:10.1029/2002JD003273, 2003.

Thorncroft, C.D., D.J. Parker, R.R. Burton, M. Diop, J.H. Ayers, H. Barjat, S. Devereau, A. Diongue, R. Dumelow, D.R. Kindred, N.M. Price, M. Saloum, C.M. Taylor, and A.M. Tomkins, The JET2000 project: Aircraft observations of the African Easterly Jet and African Easterly Waves, Bulletin of the American Meteorological Society, 84, 3, 337-351, 2003.

Volz, F.E., Infrared optical constants of ammonium sulphate, Sahara dust, volcanic pumice and flyash, Applied Optics, 12 (3), 564-567, 1973.

Wielicki, B. A., B. R. Barkstrom, E. F. Harrison, R. B. Lee III, G. L. Smith, and J. E. Cooper, 1996: Clouds and the Earth's Radiant Energy System (CERES): An Earth observing system experiment. Bull. Amer. Meteorol. Soc., 77, 853-868.

World Climate Program (WCP), A Preliminary Cloudless Standard Atmosphere for Radiation Computation, World Meterolo. Organ., Geneva, 1986.

Zhang, J., and S.A. Christopher, Longwave radiative forcing of Saharan dust aerosols from MODIS, MISR, and CERES observations on Terra, Geophys. Res. Lett., 30(23), 2188, doi:10.1029/2003GL018479, 2003.

**Figure Captions**

**Figure 1. The July 2003 monthly mean a) $OLR_{GERB}$, b) OLRmodel c) OLRmodel-$OLR_{GERB}$. The monthly mean consists of the average of the monthly mean of the OLR diagnosed at 0UTC, 6UTC, 12UTC, and 18UTC. Units are Wm-2.**

**Figure 2. The July 2003 monthly mean of the 12UTC clear-sky a) $OLRc_{GERB}$, b) $OLRc_{model}$ c) $OLRc_{model}$-$OLRc_{GERB}$. Units are $Wm^{-2}$. Areas shown in white indicate missing/cloudy data. The approximate positions of the radiosonde stations, measurement campaigns, and AERONET sites referred to in the text are also shown.**

**Figure 3. Tephigrams showing the vertical profiles of temperature and humidity for a) In Salah, b) Tindouf, c) Tamanrasset, d) JET-2000. The NWP model data are shown by the symbols in a-c.**

**Figure 4. a) The surface skin temperature, Ts, from the NWP model, b) The reduction in the model temperature required to explain the difference between $OLRc_{model}$ and $OLRc_{GERB}$, c) The model Ts required so that $OLRc_{model}$ fits $OLRc_{GERB}$ . Units K.**

**Figure 5. The diurnal variation of Ts (K) shown every 3-hours. The solid curve shows the fit from the parameterisation of Göttsche and Olesen [2001] and the values for the fitting parameters are indicated.**

**Figure 6. The aerosol size distribution used to calculate the Saharan dust optical properties. The stars represent measurements from the PCASP-100X, and the diamonds represent the monthly mean aerosol size distribution retrieved from the AERONET site at Dahkla. The 5 modes that are used to fit the aerosol size distribution are also shown.**

**Figure 7. The aerosol optical parameters calculated using the size distribution shown in Fig 3, and the refractive indices described in the text. a) specific extinction coefficient, $k_e$, in units of $m^2g^{-1}$; the crosses show the wavelength dependence of the monthly mean aerosol optical depth calculated from the AERONET site. b) single scattering albedo, $\omega_o$; the crosses show the monthly mean $\omega_o$ determined from the AERONET site. c) asymmetry factor, g.**

**Figure 8. $\tau_{aer0.55}$ derived for July 2003 for a) TOMS, b) MISR. In deriving the $\tau_{aer0.55}$ from TOMS, the TOMS AI is related to $\tau_{aer0.44}$ via equation (1), and the wavelength dependence of $k_e$ shown in Figure 4a is used to derive $\tau_{aer0.55}$ via equation (2). $\tau_{aer0.55}$ may be related to $\tau_{aer10}$ by equation (3).**

**Figure 9. A scatter-plot showing the correlation between $\tau_{aer0.55}$ from TOMS and $\tau_{aer0.55}$ from MISR.**

**Figure 10. Graphical representation of the look-up-table for determining $DRE_{LW}$. The x-axis shows the surface temperature, and the y-axis shows the top of the atmosphere clear sky *OLRc*. $DRE_{LW}$ may be determined by $OLRc_{no\_aer}$- $OLRc_{aer}$.**

**Figure 11. $DRE_{LW}$ due to the radiative effect of mineral dust ($Wm^{-2}$).**

**Figure 12. Graphical representation of the look-up-table for determining the ratio of $SW_{surf\_aer}$ to $SW_{surf\_no\_aer}$ and hence DRELW_feedback as described in the text.**

**Figure 13. The change in model Ts (K) due to the reduction in SWsurf.**

**Figure 14. $DRE_{LW}$+ $DRE_{LW\_feedback}$ ($Wm^{-2}$), which represents our best estimate of the radiative effect of mineral dust in the terrestrial spectrum.**

Figures

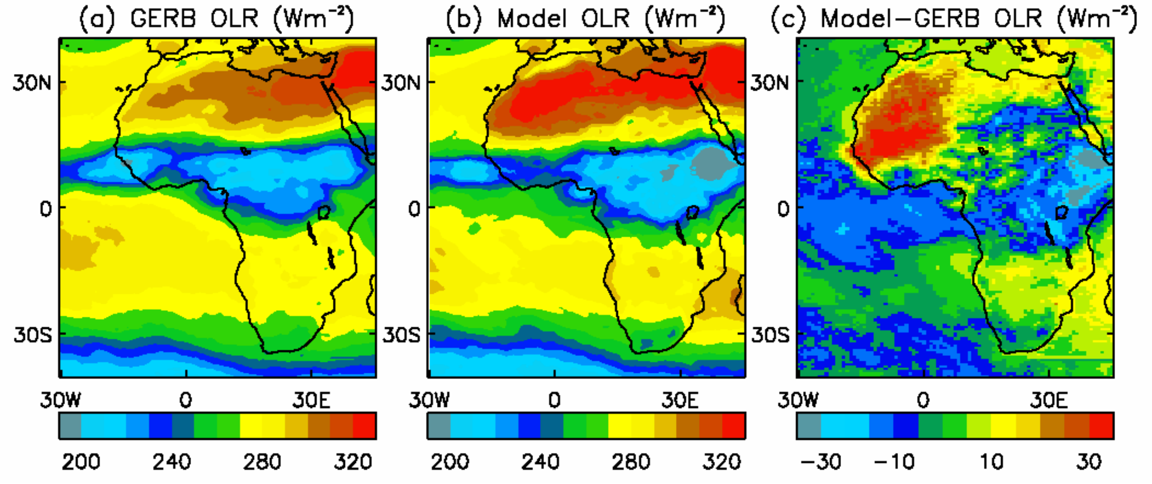

Fig1

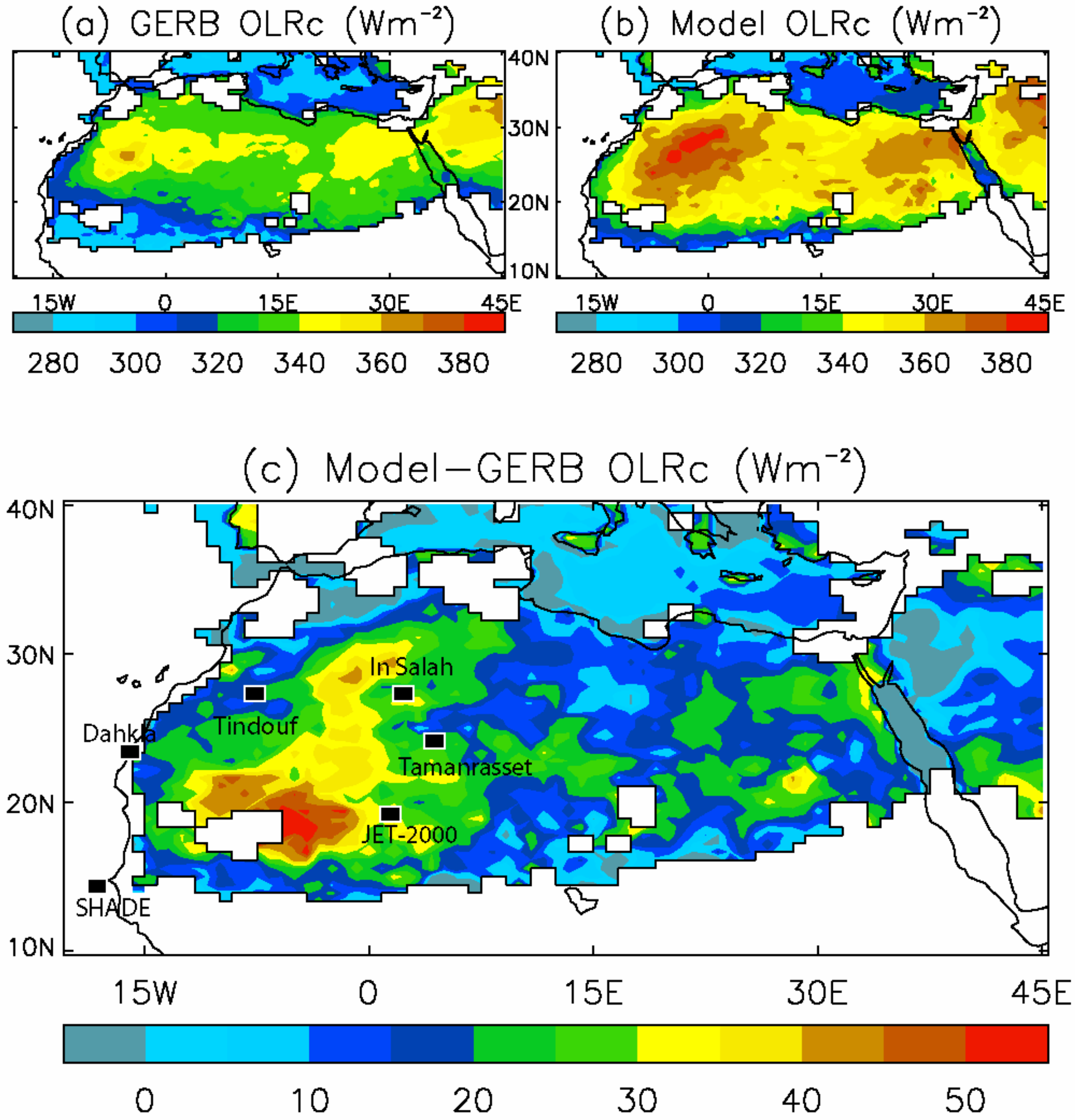
(a) GERB OLRc (Wm$^{-2}$)
(b) Model OLRc (Wm$^{-2}$)
40N
30N
20N
10N
15W
0
15E
30E
45E
280
300
320
340
360
380
(c) Model−GERB OLRc (Wm$^{-2}$)
In Salah
Tindouf
Dahkla
Tamanrasset
JET-2000
SHADE
0
10
20
30
40
50

Fig2

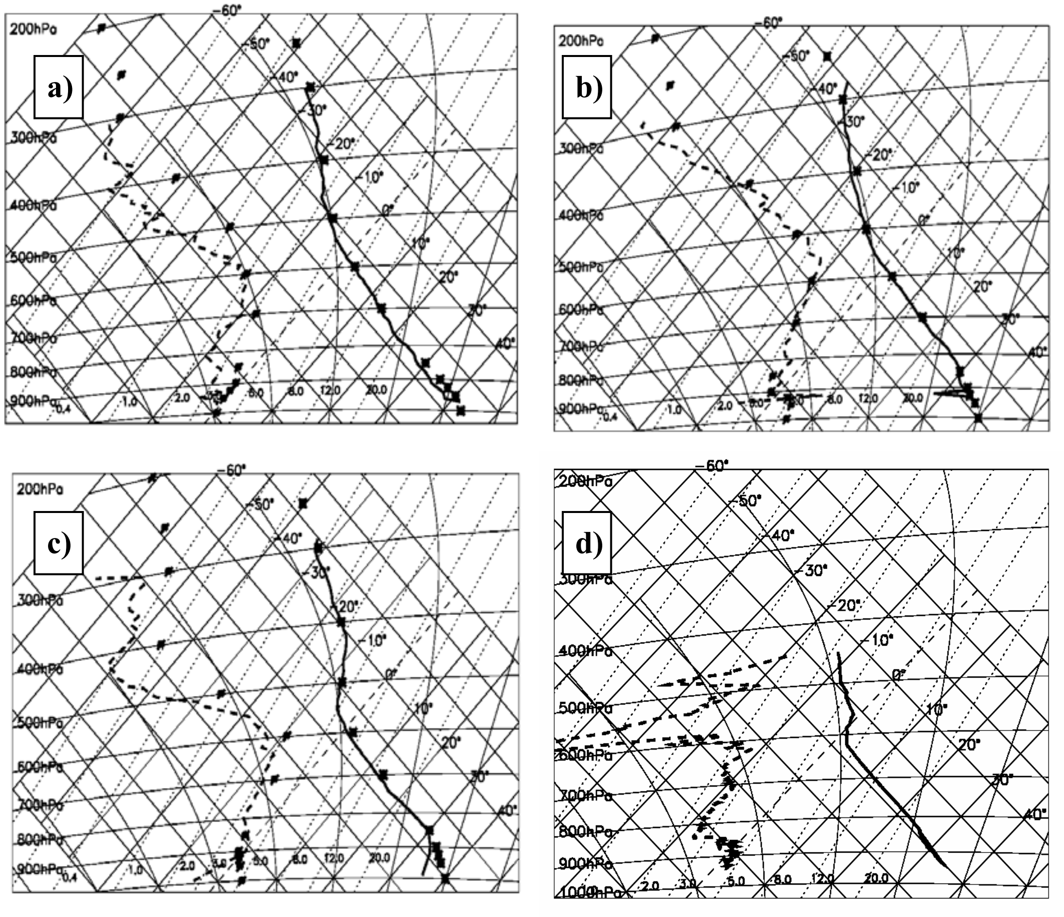
a)
b)
c)
d)
200hPa
300hPa
400hPa
500hPa
600hPa
700hPa
800hPa
900hPa
1000hPa
-60°
-50°
-40°
-30°
-20°
-10°
0°
10°
20°
30°
40°
0.4
1.0
2.0
3.0
5.0
8.0
12.0
20.0

Fig 3

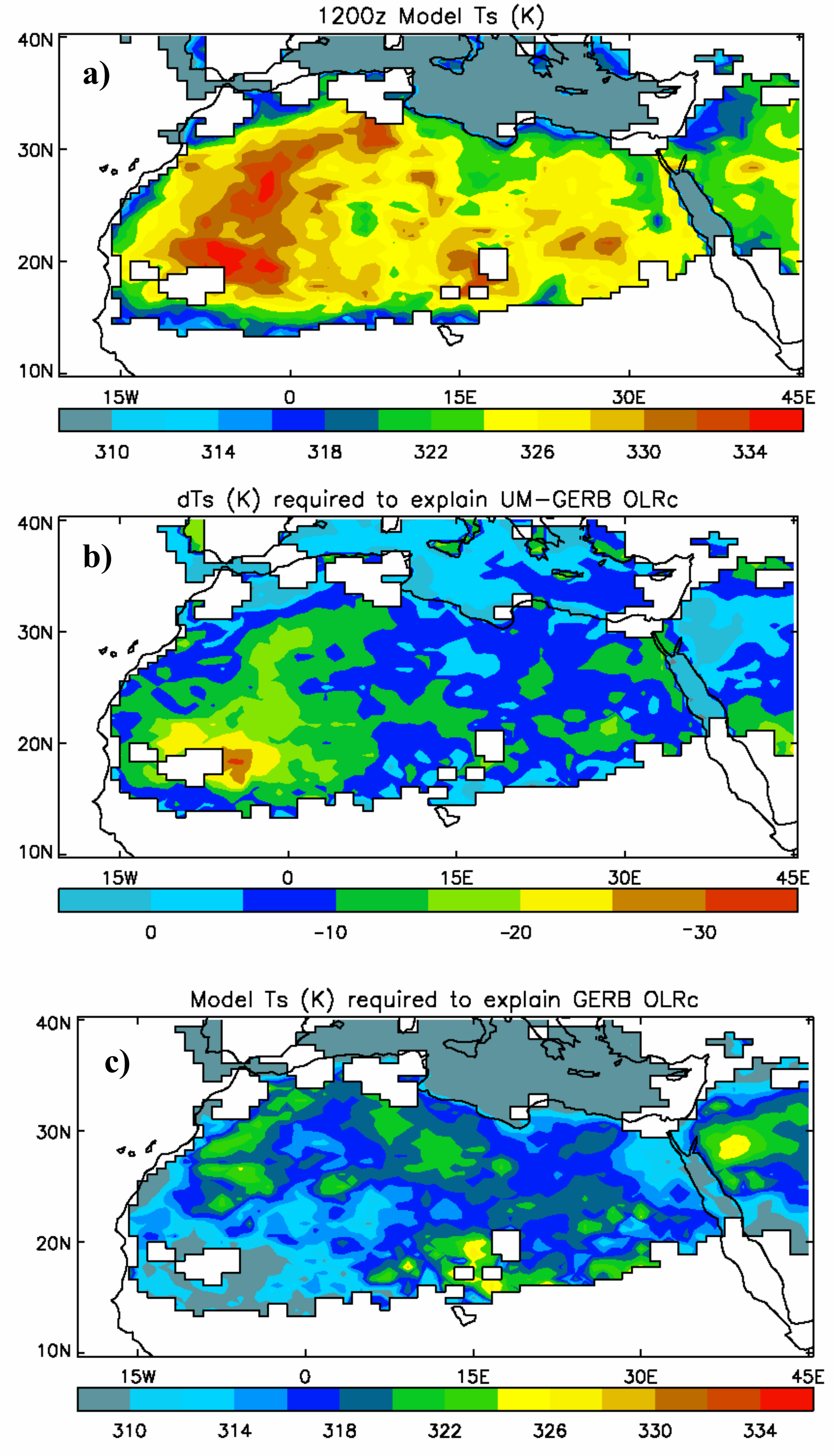
1200z Model Ts (K)
a)
40N
30N
20N
10N
15W
0
15E
30E
45E
310
314
318
322
326
330
334
dTs (K) required to explain UM−GERB OLRc
b)
40N
30N
20N
10N
15W
0
15E
30E
45E
0
−10
−20
−30
Model Ts (K) required to explain GERB OLRc
c)
40N
30N
20N
10N
15W
0
15E
30E
45E
310
314
318
322
326
330
334

Fig 4.

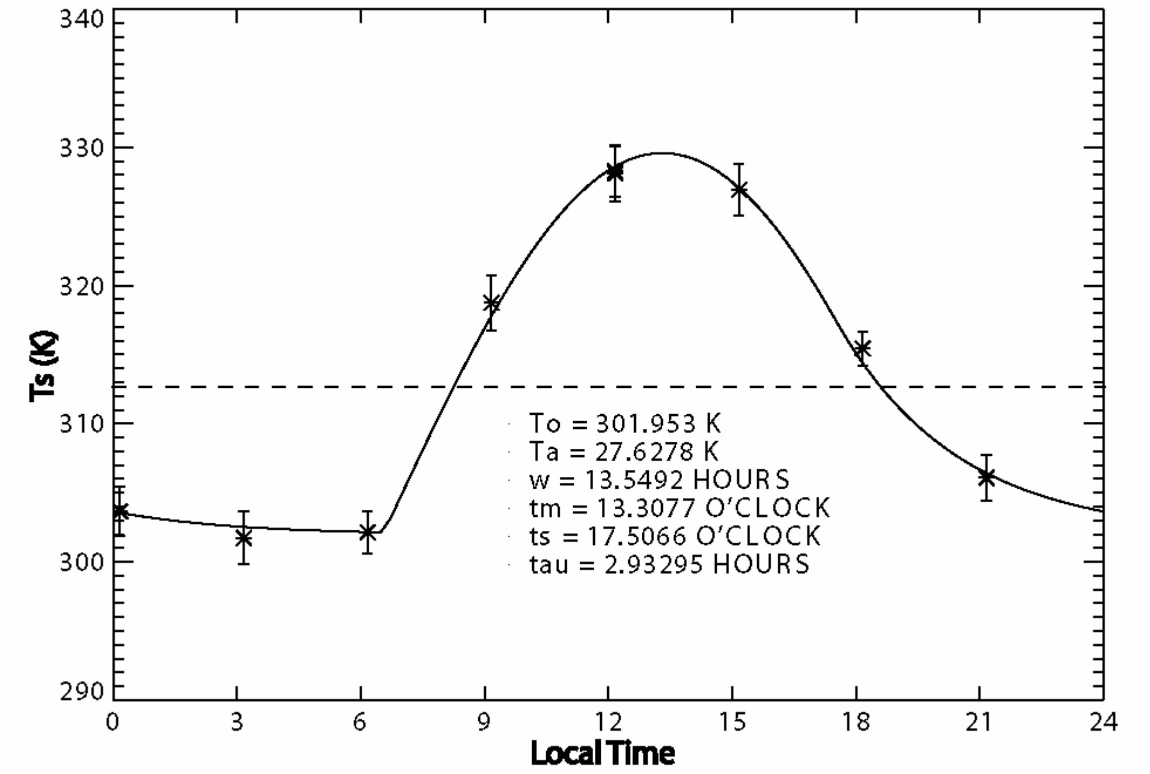

340
330
320
310
300
290
Ts (K)
0
3
6
9
12
15
18
21
24
Local Time
To = 301.953 K
Ta = 27.6278 K
w = 13.5492 HOURS
tm = 13.3077 O'CLOCK
ts = 17.5066 O'CLOCK
tau = 2.93295 HOURS

Figure 5.

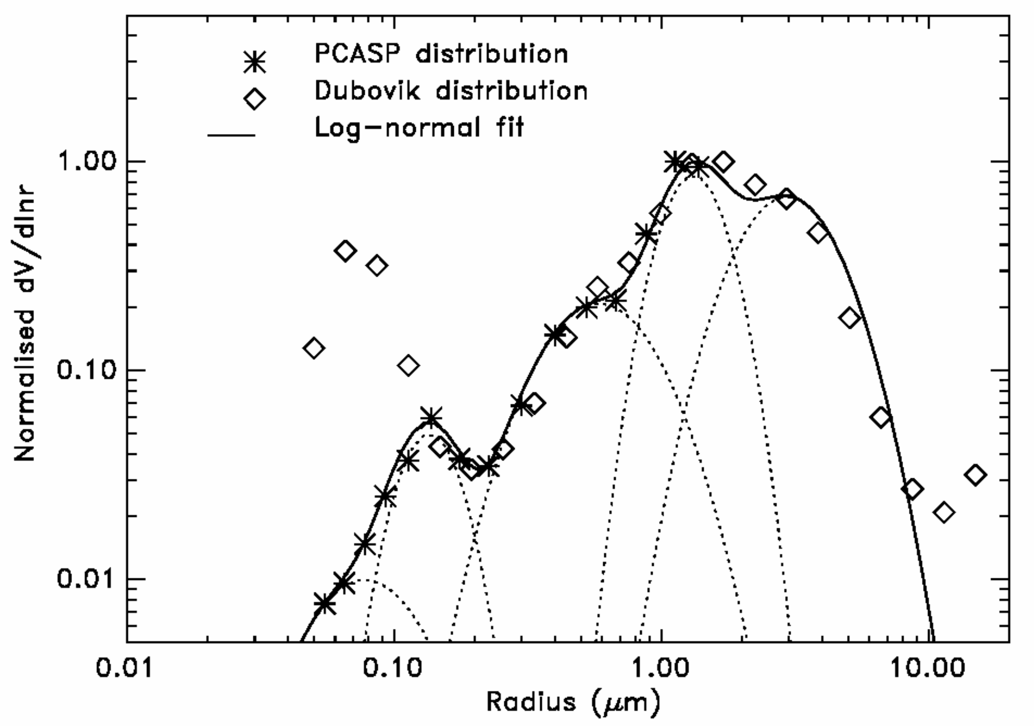
PCASP distribution
Dubovik distribution
Log-normal fit
Normalised dV/dlnr
1.00
0.10
0.01
0.01
0.10
1.00
10.00
Radius (μm)

Fig 6

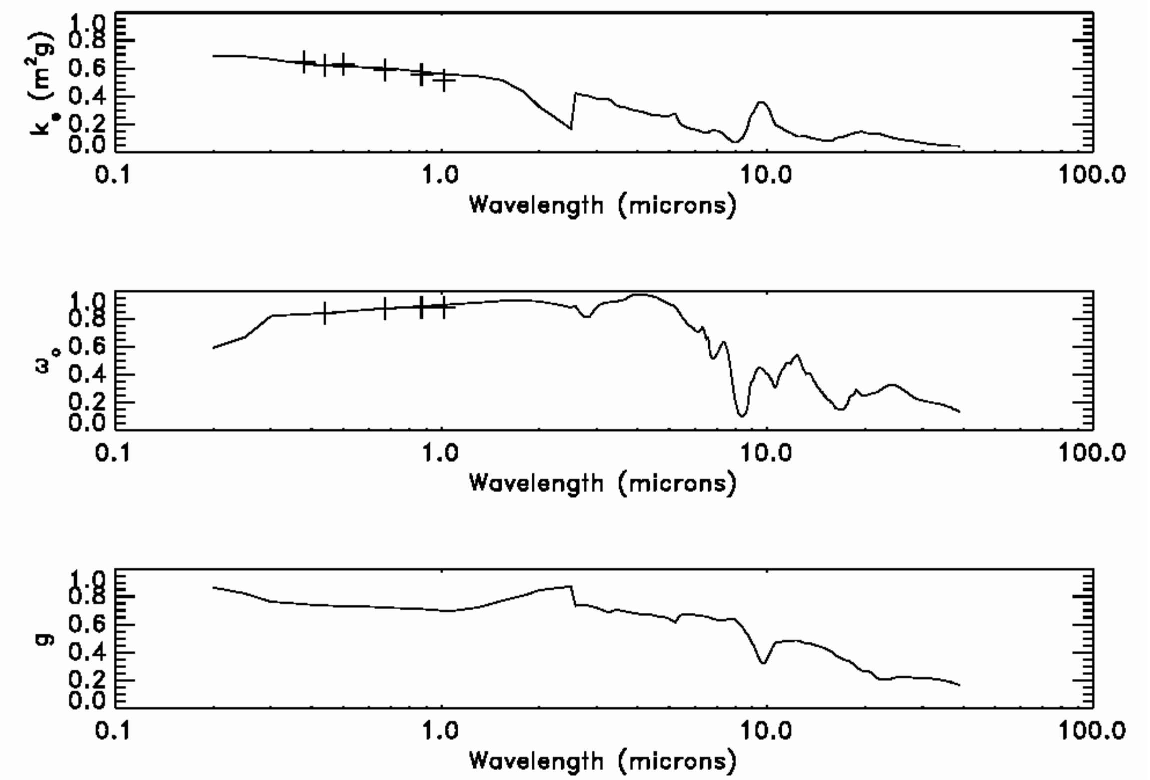

$k_e$ ($m^2$g)
1.0
0.8
0.6
0.4
0.2
0.0
0.1
1.0
10.0
100.0
Wavelength (microns)
$\omega_o$
g

Fig 7.

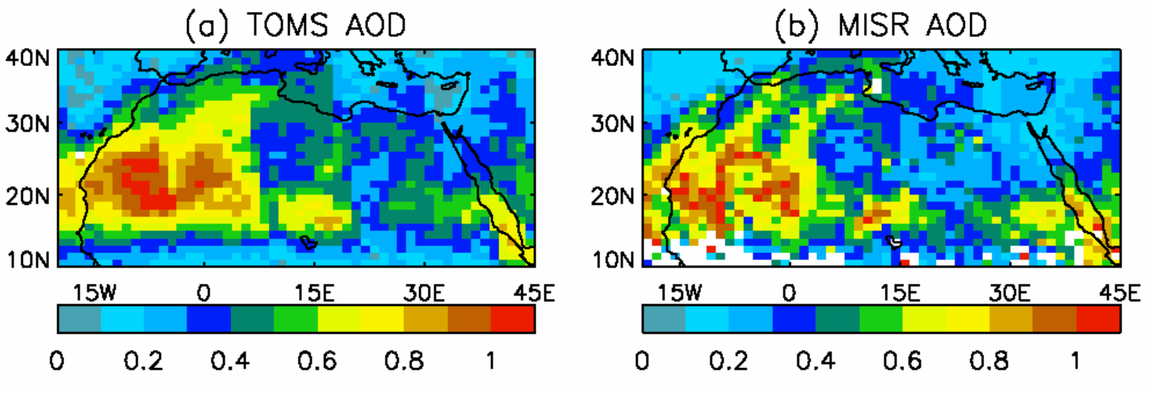
(a) TOMS AOD
(b) MISR AOD
40N
30N
20N
10N
15W
0
15E
30E
45E
0
0.2
0.4
0.6
0.8
1

Fig 8

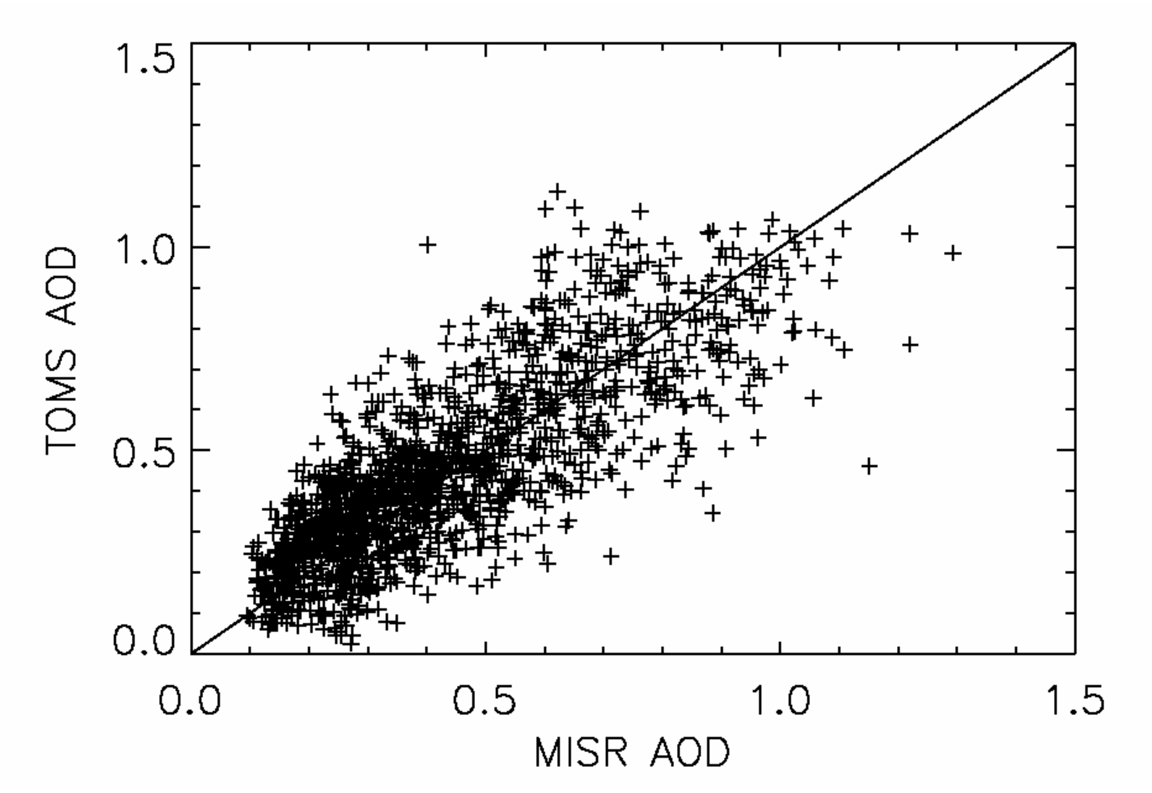
1.5
1.0
0.5
0.0
TOMS AOD
0.0
0.5
1.0
1.5
MISR AOD

Fig 9

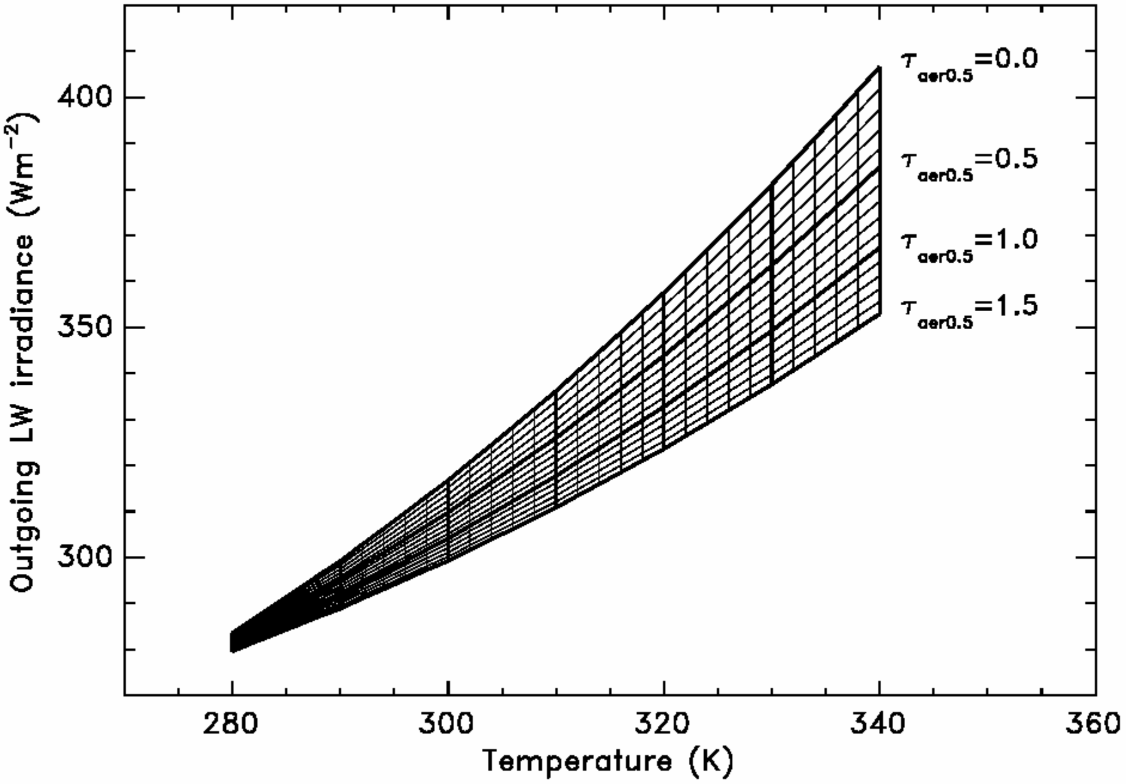

$\tau_{aer0.5}=0.0$
$\tau_{aer0.5}=0.5$
$\tau_{aer0.5}=1.0$
$\tau_{aer0.5}=1.5$
Outgoing LW irradiance ($Wm^{-2}$)
400
350
300
280
300
320
340
360
Temperature (K)

Fig 10

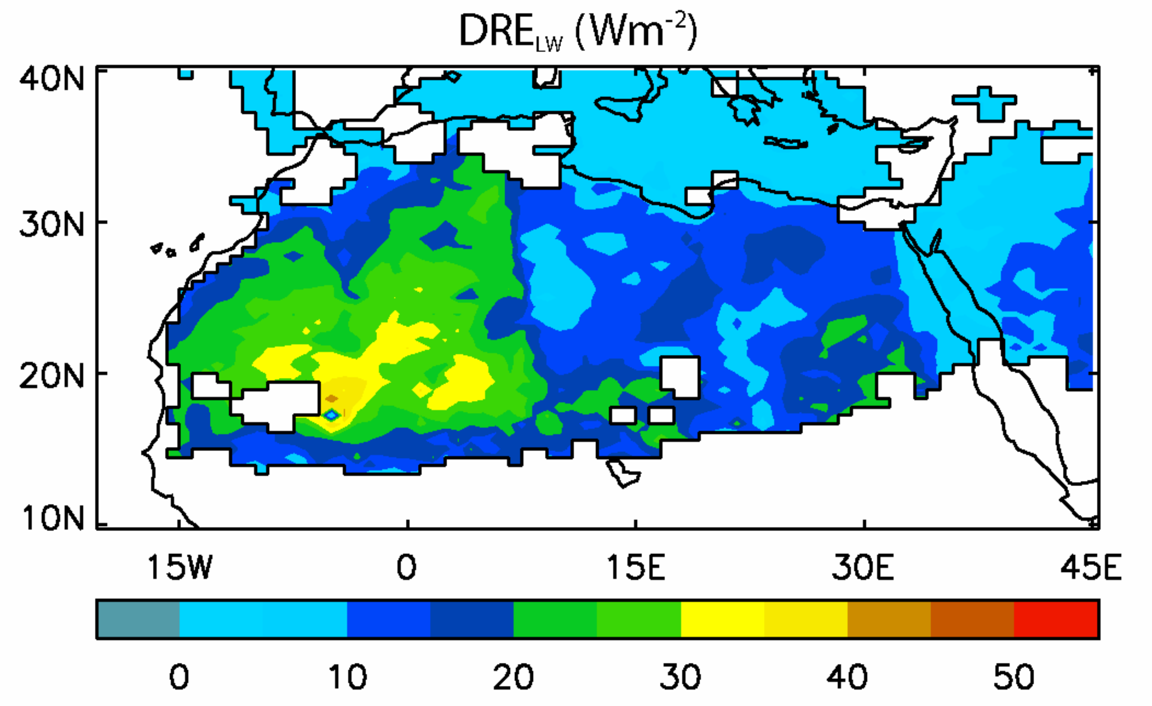

Fig 11

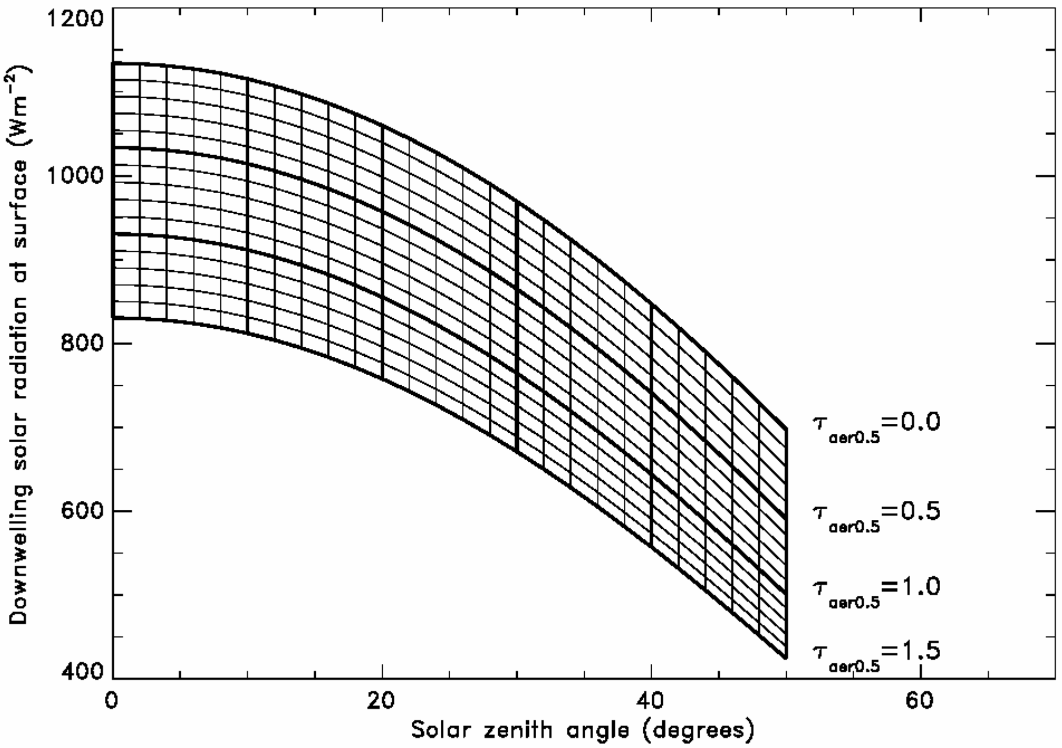
Downwelling solar radiation at surface (Wm$^{-2}$)
1200
1000
800
600
400
0
20
40
60
Solar zenith angle (degrees)
$\tau_{aer0.5}$=0.0
$\tau_{aer0.5}$=0.5
$\tau_{aer0.5}$=1.0
$\tau_{aer0.5}$=1.5

Fig 12

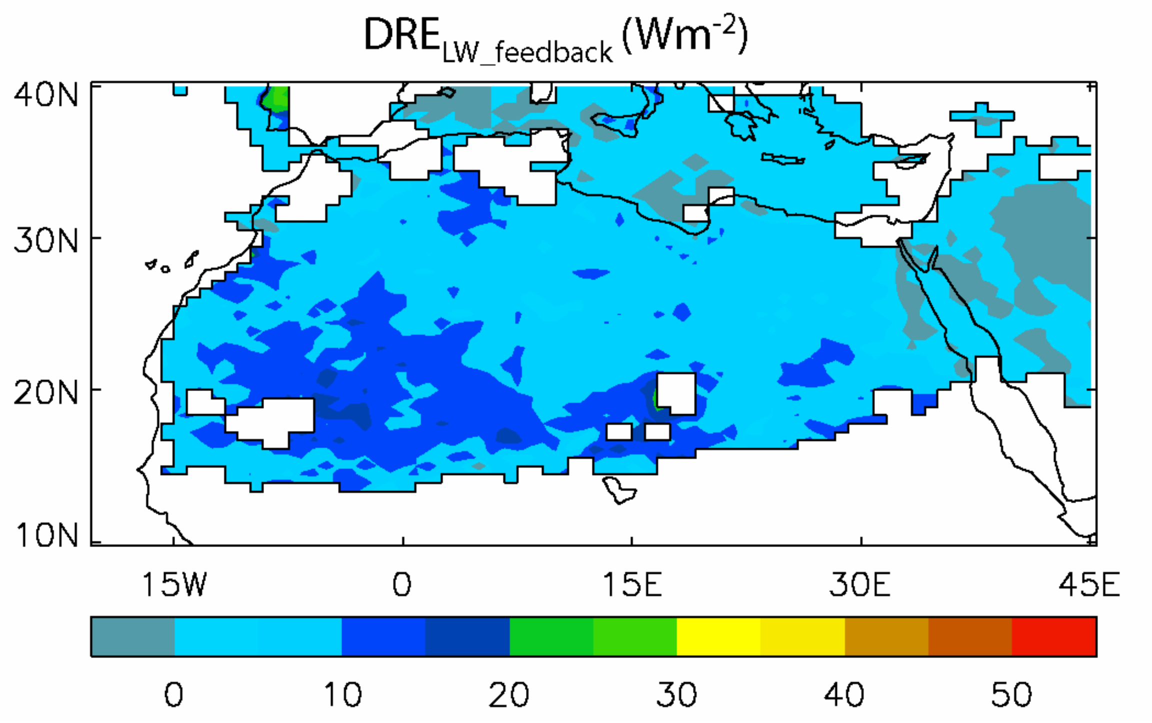

$DRE_{LW\_feedback}$ ($Wm^{-2}$)
40N
30N
20N
10N
15W
0
15E
30E
45E
0
10
20
30
40
50

Figure 13.

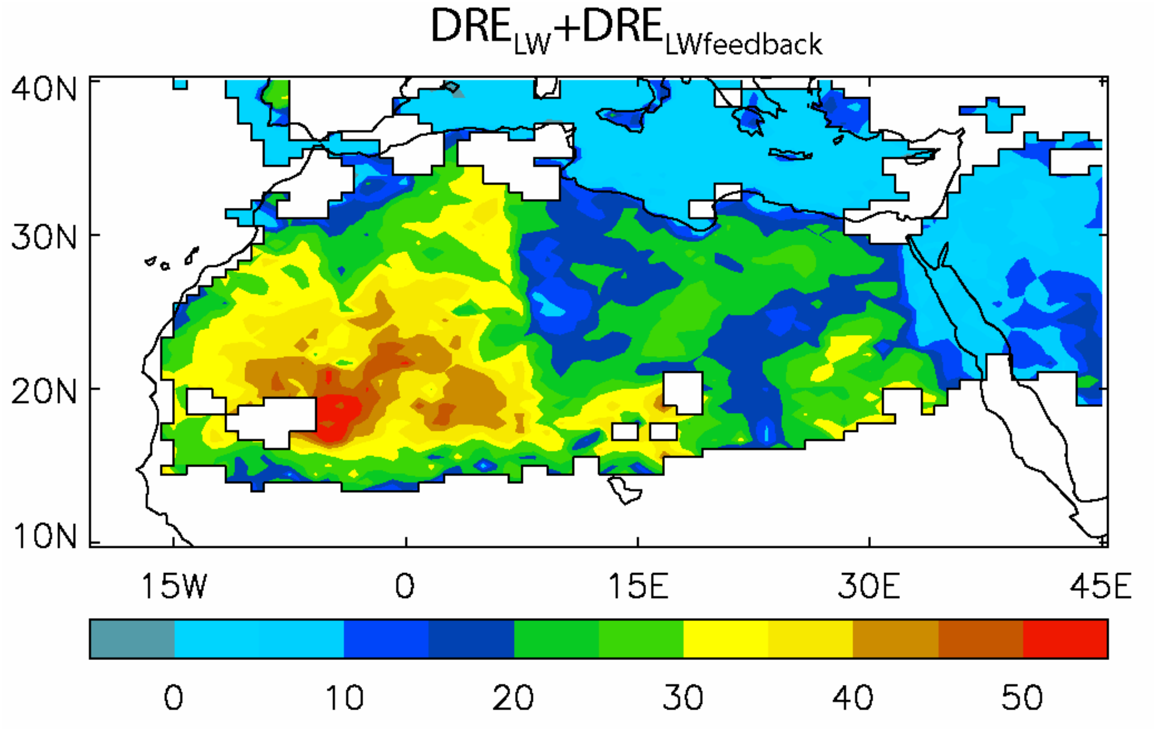
$DRE_{LW}+DRE_{LWfeedback}$
40N
30N
20N
10N
15W
0
15E
30E
45E
0
10
20
30
40
50

Fig 14.